Compressible Navier-Stokes analysis of floating wind turbine rotor aerodynamics

Proceedings of IOWTC 2018
ASME 2018 1st International Offshore Wind Technical Conference
November 4-7, 2018, San Francisco, CA

IOWTC2018-1059

COMPRESSIBLE NAVIER-STOKES ANALYSIS OF FLOATING WIND TURBINE ROTOR AERODYNAMICS

M. Sergio Campobasso[*]
Andrea G. Sanvito[†]
University of Lancaster, Department of Engineering
Lancaster LA1 4YR, United Kingdom

Jernej Drofelnik[‡]
University of Southampton,
Faculty of Engineering and the Environment
Southampton SO17 1BJ, United Kingdom

Adrian Jackson[§]
University of Edinburgh, EPCC
Edinburgh EH9 3JZ, United Kingdom

Yang Zhou[¶]
Qing Xiao[‖]
University of Strathclyde,
Naval Architecture, Ocean and Marine Engineering
Glasgow G4 0LZ, United Kingdom

Alessandro Croce[**]
Politecnico di Milano, Department of Aerospace Engineering
20156 Milano, Italy

ABSTRACT

The unsteady aerodynamics of floating offshore wind turbine rotors is more complex than that of fixed-bottom turbine rotors, due to additional rigid-body motion components enabled by the lack of rigid foundations; it is still unclear if low-fidelity aerodynamic models, such as the blade element momentum theory, provide sufficiently reliable input for floating turbine design requiring load data for a wide range of operating conditions. High-fidelity Navies-Stokes CFD has the potential to improve the understanding of FOWT rotor aerodynamics, and support the improvement of lower-fidelity aerodynamic analysis models. To accomplish these aims, this study uses an in-house compressible Navier-Stokes code and the NREL FAST engineering code to analyze the unsteady flow regime of the NREL 5 MW rotor pitching with amplitude of 4^o *and frequency of* 0.2 *Hz, and compares all results to those obtained with a commercial incompressible code and FAST in a previous independent study. The level of agreement of CFD and engineering analyses in each of these two studies is found to be quantitatively similar, but the peak rotor power of the compressible flow analysis is about* 20 *% higher than that of the incompressible analysis. This is possibly due to compressibility effects, as the instantaneous local Mach number is found to be higher than* 0.4*. Validation of the compressible flow analysis set-up, using an absolute frame formulation and low-speed preconditioning, is based on the analysis of the steady and yawed flow past the NREL Phase VI rotor.*

[*]Email: m.s.campobasso@lancaster.ac.uk. Corresponding author
[†]Email: a.sanvito@lancaster.ac.uk
[‡]Email: j.drofelnik@soton.ac.uk
[§]Email: adrian.jackson@ed.ac.uk
[¶]Email: yang.zhou@strath.ac.uk
[‖]Email: qing.xiao@strath.ac.uk
[**]Email: alessandro.croce@polimi.it

INTRODUCTION

Wind energy is playing an increasingly crucial role in lowering greenhouse gas emissions due to electricity generation, and,

in this sector, is now regarded as one of the most cost–effective climate change mitigation technologies. Utility–scale horizontal axis wind turbines (HAWTs) with 8 MW rated power and blade length in the region of 80 meters are due to enter service in the very near future. Due to the spatial and temporal variability of the environmental conditions, HAWTs regularly experience unsteady flow conditions which induce fatigue and lower the energy harvest. Most of such regimes arise from aerodynamic unsteadiness of the flow field past the rotor blades, typically due to: a) turbulence of the oncoming wind, b) turbulence due to heat transfer between ground and air in thermally unstable atmosphere, c) vertical gradients of the wind speed due to the atmospheric boundary layer, d) variable pressure field due to the downwind tower of upwind rotors, and e) yawed wind, occurring when wind speed and rotor normal are misaligned.

These phenomena affect both onshore and fixed-bottom offshore HAWTs. In the case of floating offshore wind turbines (FOWTs), an additional significant source of rotor flow unsteadiness arises from the motion of the turbine floater [1]. The entire turbine undergoes a rigid-body motion determined by the dynamic equilibrium of the aerodynamic forces on the rotor, the hydrodynamic forces on the floater, the constraining loads of the mooring system and the inertial forces of the turbine/floater ensemble. Assessing reliably the effects of FOWT motion on rotor unsteady aerodynamics is key to determining design-driving fatigue loads. In turn, reliable predictions of rotor unsteady aerodynamics, as well as floater hydrodynamics and whole-structure aeroelasticity, are essential for assessing the overall hydrodynamic stability of the FOWT system and designing its control.

Thus, HAWT design is a complex multidisciplinary task involving rotor aerodynamics, structure mechanics, aeroelasticy, controls and, in the FOWT case, also floater hydrodynamics and mooring dynamics. Predicting with sufficient reliability turbine rotor aerodynamics is paramount to wind turbine design. Current design codes largely rely on low–fidelity methods such as the blade element momentum theory (BEMT), augmented with semi–empirical extensions such dynamic stall models [2]. These codes are extremely fast and, thus, ideally suited to industrial design, but their predictions may be affected by significant uncertainty when dealing with complex three–dimensional (3D) rotor flows. For example, the uncertainty affecting the prediction of low-fidelity codes for yawed flows is discussed in [3], and studies providing quantitative comparisons of BEMT and high-fidelity Navier-Stokes (NS) Computational Fluid Dynamics (CFD) predictions are cited therein. The use of BEMT-based engineering codes for FOWT analysis entails additional uncertainty, due to the, generally non-uniform, time-dependent entrainment velocity associated with the rigid–body motion of the whole turbine, which introduces further complexity in rotor unsteady aerodynamics. Relatively large FOWT oscillatory motion may result in the rotor interacting with its own wake [4] (vortex ring state), a phenomenon unlikely to be resolved sufficiently well by BEMT. A more general discussion of the potential uncertainty affecting BEMT predictions of FOWT rotor aerodynamics is reported in [5].

Recent studies using both NS CFD and BEMT-based engineering codes investigate the correlation between the results of high-fidelity CFD and BEMT-based codes. Comparisons of FOWT unsteady aerodynamic predictions using BEMT-based codes and NS CFD were made by Tran and Kim, who used the FLUENT incompressible flow solver with the multiple reference frame set-up (use of this modeling feature avoids the need for moving computational grids) to investigate the rotor aerodynamics of pitching FOWTs [4], finding a good agreement of the two approaches for small pitching amplitudes, and differences of power and thrust of up to 24 % for pitching amplitude of 4^o; the same authors later used the STAR-CCM+ code with overset grids and BEMT codes to investigate FOWT rotor unsteady aerodynamics due to prescribed platform surge [6]. Thereafter they used a strongly coupled aerodynamic/hydrodynamic high-fidelity CFD system and the NREL wind turbine engineering code FAST [7] to investigate more general FOWT motions [8], finding that the level of agreement between high- and low-fidelity predictions worsened with the severity of the operating condition. Liu *et al.* [9] used a high-fidelity multi-disciplinary strongly coupled system based on OpenFOAM and including rotor aerodynamics, platform hydrodynamics and mooring dynamics to analyze whole-system FOWT dynamics, and compared their high-fidelity simulations to FAST predictions, reporting an overall good agreement between the two approaches for the considered cases. One of the merits of the aforementioned studies is that they also investigate the dependence of the correlation between low- and high-fidelity predictions on operating conditions. This knowledge can be used to further improve engineering code predictions and/or their usage, for example by improving the choice of FOWT configuration– and regime–dependent safety factors, and/or improving aerodynamic modeling aspects.

However, uncertainty sources also exist in NS CFD for wind turbine aerodynamics. Other than the long–standing challenge of reliably resolving stall in a wide range of diverse operating conditions, and the lack of measured data to validate the NS predictions of the interaction of a rotor with its own wake in the FOWT framework, one may also ask if the additional time-dependent non-uniform entrainment velocities of FOWT floaters may not yield significant flow compressibility effects. If so, neglecting such effects may result in significant errors affecting CFD FOWT performance analysis. Compressible NS CFD is already used for both fixed-bottom HAWT and FOWT aerodynamics [10, 11], but there is still no strong justification for preferring either approach.

The main objectives of this study are to a) investigate the existence and impact of compressibility effects in FOWT rotor aerodynamics, b) discuss important but often overlooked numerical aspects of NS CFD codes used for analyzing FOWT rotor aerodynamics, with particular emphasis on the calculation of grid

valocities, and c) provide a novel contribution to the analysis of the correlation between low- and high-fidelity technologies for FOWT rotor aerodynamics by analyzing with compressible flow CFD and an engineering code a pitching FOWT test case analyzed with incompressible flow CFD and engineering codes in a previous independent study. The formulation of the Navier-Stokes equations in the absolute reference frame and the rotating frame attached to turbine rotors is presented first. This is followed by a section on the formulation of grid velocities for fixed-bottom and pitching turbine rotors. The main features of the compressible NS CFD Optimized Structured multi–block Algorithm (COSA) code used herein are then briefly described, with emphasis on the options available for discretizing the grid cell face velocities, and low-speed preconditioning, a numerical method required in compressible NS solvers when dealing with flows containing regions of low-speed flows. Novel verification and validation analyses, based on the analysis of steady and yawed flow regimes of the NREL Phase VI rotor [12] are then provided. The following main results refer to a FOWT featuring the NREL 5 MW reference turbine [13] and pitching with amplitude of 4^o and frequency of 0.2 Hz, and include detailed COSA unteady flow analyses and cross comparisons of the integral output of COSA and FAST. A summary and future perspectives are provided in the closing section.

GOVERNING EQUATIONS

The 3D compressible RANS equations are a system of conservation laws expressing the conservation of mass, momentum and energy in a turbulent fluid flow. In the RANS model framework, the mean effects of turbulence on the flow field are accounted for by introducing the Reynolds stress tensor in the momentum and energy equations. In the COSA code used in this study, the Reynolds stress tensor is modelled using a linear eddy viscosity model, namely Menter's two–equation $k-\omega$ shear stress transport (SST) turbulence model [14, 15]. Thus, turbulent compressible flows are determined by solving a system of $N_{pde} = 7$ partial differential equations (PDEs) and an equation of state linking fluid density, pressure and internal energy. Although compressibility effects in HAWT flows may presently be relatively small, due to the blade tip speed of modern HAWTs not exceeding the Mach 0.3 threshold, the compressible flow formulation was adopted in COSA to develop and maintain a single code for both low–speed [16] and high–speed [17] problems.

Given a moving control volume C with boundary S, the Arbitrary Lagrangian–Eulerian (ALE) integral form of the system of the time–dependent (TD) RANS and SST equations in a stationary (*i.e.* absolute) Cartesian coordinate system is:

$$\frac{\partial}{\partial t}\left(\int_{C(t)} \mathbf{U} dC\right) + \oint_{S(t)} (\underline{\Phi}_c - \underline{\Phi}_d)\cdot d\underline{S} - \int_{C(t)} \mathbf{S}_A dC = 0 \quad (1)$$

where $\mathbf{U} = [\rho \quad \rho\underline{u}^T \quad \rho E \quad \rho k \quad \rho\omega]^T$ is the array of conservative variables, the superscript T denotes the transpose operator, and the symbols ρ, $\underline{u}$, E, k and ω denote respectively density, absolute velocity vector, and total energy, turbulent kinetic energy and specific dissipation rate of turbulent kinetic energy per unit mass. The total energy is $E = e + (\underline{u}\cdot\underline{u})/2 + k$, where e denotes the internal energy per unit mass; the perfect gas law is used to express the static pressure p as a function of ρ, E, k and the mean flow kinetic energy per unit mass $(\underline{u}\cdot\underline{u})/2$ [15]. The generalized convective flux vector $\underline{\Phi}_c$ is:

$$\underline{\Phi}_c = \begin{bmatrix} \rho(\underline{u}-\underline{u}_b)^T \\ \rho(\underline{u}-\underline{u}_b)^T\underline{u} + pI \\ \rho E(\underline{u}-\underline{u}_b)^T + p\underline{u}^T \\ \rho k(\underline{u}-\underline{u}_b)^T \\ \rho\omega(\underline{u}-\underline{u}_b)^T \end{bmatrix} \quad (2)$$

where I is the (3×3) identity matrix, and $\underline{u}_b$ is the boundary velocity. When the control volume represents one cell of the rotating grid attached to a fixed-bottom HAWT rotor, $\underline{u}_b$ is given by:

$$\underline{u}_b = \underline{\Omega}\times\underline{r} \quad (3)$$

in which $\underline{r}$ denotes the time-dependent position vector in the absolute frame with respect to a point on the rotational axis, and $\underline{\Omega}$ is the rotor angular speed.

The definition of the generalized diffusive flux vector $\underline{\Phi}_d$ is reported in [15, 18], and the source term $\mathbf{S}_A$ is given by:

$$\mathbf{S}_A = \begin{bmatrix} 0 & \underline{0}^T & 0 & S_k & S_\omega \end{bmatrix}^T \quad (4)$$

where S_k and S_ω denote respectively the source terms of the k and ω equations of the SST turbulence model [16].

In many applications involving rotational body motion, such as turbomachinery, helicopter and HAWT rotor flows, it is convenient to formulate the governing equations in a rotating (*i.e.* relative) frame of reference. In simple cases, such as the analysis of the flow field of a fixed-bottom HAWT rotor in uniform wind normal to the rotor plane, this enables solving a problem that is unsteady in the stationary frame as a steady problem in the rotating frame. Moreover, in the case of unsteady periodic rotor flows, the choice of the relative frame formulation enables the use of frequency-domain perturbation methods, such as the harmonic balance Navier-Stokes method, to greatly accelerate the runtime of the analysis of periodic HAWT flows [3].

Solving the governing equations in the relative frame, the grid position remains unaltered during the simulation. When formulating the governing equations in the rotating frame, one can

express the relative flow velocity vector either in the relative or the absolute frame [19]. The two formulations are mathematically equivalent, but representing the relative fluid velocity in the absolute frame is numerically more convenient for open rotor applications. Using an absolute frame representation of the relative velocity of the fluid, the counterpart of System (1) in a Cartesian rotating frame is found to be:

$$\frac{\partial}{\partial t}\left(\int_C \mathbf{U} dC\right) + \oint_S (\underline{\Phi}_c - \underline{\Phi}_d)\cdot d\underline{S} - \int_C \mathbf{S}_R dC = 0 \qquad (5)$$

The expressions of $\mathbf{U}$, $\underline{\Phi}_c$, and $\underline{\Phi}_d$ in Eq. (5) are identical to those in Eq. (1). However, the control volume C and its boundary S are no longer time-dependent. The expression of the source $\mathbf{S}_R$ differs from that of $\mathbf{S}_A$ because of additional terms depending on the Coriolis force, and is given by:

$$\mathbf{S}_R = \begin{bmatrix} 0 & \rho(\underline{\Omega}\times\underline{\mathrm{u}})^T & 0 & S_k & S_\omega \end{bmatrix}^T \qquad (6)$$

It is emphasized that the source term depending on Ω in Eq. (6) and the face velocities of the grid cells $\underline{\mathrm{u}}_b$ in Eq. (2) are nonzero also for steady rotor flows. When using the relative frame formulation of System (5) to solve unsteady HAWT rotor flows, the unsteady excitation is enforced through modified time-dependent farfield boundary conditions in the case of unsteadiness due to misaligned and/or nonuniform and/or time-dependent wind [3]; the unsteady excitation due to angular motion components of FOWT towers (*e.g.* pitching, rolling and yawing) is instead enforced through additional Coriolis force source terms in the momentum equations (*i.e.* additional terms in Eq. (6)), and modified more general expressions of the boundary velocity $\underline{\mathrm{u}}_b$, as shown in the next section for the case of tower pitching. For the case of translational motion components of the tower (*i.e.* surge, heave and sway), the source term of Eq. (6) remains unaltered, and one only has to include additional translational velocity components in the expression of $\underline{\mathrm{u}}_b$.

GRID VELOCITIES

In the COSA code, fixed-bottom HAWT rotors rotate about the z axis with constant angular velocity $\underline{\Omega}$, and the time-dependent x- and y-coordinates of a grid point are:

$$x_r = x_0 + (x_0 - x_{rot})(c-1) - (y_0 - y_{rot})s \qquad (7)$$
$$y_r = y_0 + (x_0 - x_{rot})s + (y_0 - y_{rot})(c-1) \qquad (8)$$

where x_{rot} and y_{rot} are respectively the x- and y-coordinates of a point on the rotational axis, x_0 and y_0 are respectively the x- and y-coordinates of a grid point at time $t = 0$, $c = \cos\theta_r$, $s = \sin\theta_r$, and $\theta_r = \Omega t$ is the azimuthal position of a reference blade (blade 1). In all TD analyses below, the axis of one blade is vertical and above the rotor center at $t = 0$, and the angle θ_r is measured in the direction of the rotor speed from abovesaid reference angular position. The time-dependent x- and y- components of the grid point velocity, are obtained by taking the time-derivative of Equations (7) and (8), and are:

$$\dot{x}_r = [-(x_0 - x_{rot})s - (y_0 - y_{rot})c]\,\Omega \qquad (9)$$
$$\dot{y}_r = [(x_0 - x_{rot})c - (y_0 - y_{rot})s]\,\Omega \qquad (10)$$

Equations (9) and (10) are the scalar counterparts of Eq. (3).

In the case of the rotor of a pitching FOWT tower oscillating in the yz plane with amplitude Θ_p and angular frequency Ω_p past a pitching center of coordinates (y_{pc}, z_{pc}) according to:

$$\theta_p = \Theta_p \sin(\Omega_p t + \phi_p) \qquad (11)$$

with ϕ_p being a given phase angle between the instantaneous tower pitch angle θ_p and the rotor azimuthal position θ_r. Additional y and z displacements need to be added to those of Equations (7) and (8) due to the tower pitching motion. The expressions of the coordinates of a moving grid point become:

$$x = x_r \qquad (12)$$
$$y = y_r + (z_r - z_{pc})s_{tp} + (y_r - y_{pc})(c_{tp} - 1) \qquad (13)$$
$$z = z_r + (z_r - z_{pc})(c_{tp} - 1) - (y_r - y_{pc})s_{tp} \qquad (14)$$

where $c_{tp} = \cos\theta_p$ and $s_{tp} = \sin\theta_p$. Finally, the grid velocity components associated with concurrent rotation of the rotor and pitching of the tower, obtained by taking the time-derivative of Equations (12)-(14), are found to be:

$$\dot{x} = \dot{x}_r \qquad (15)$$
$$\dot{y} = (z_r - z_{pc})\dot{s}_{tp} + (y_r - y_{pc})\dot{c}_{tp} + \dot{y}_r c_{tp} \qquad (16)$$
$$\dot{z} = (z_r - z_{pc})\dot{c}_{tp} - (y_r - y_{pc})\dot{s}_{tp} - \dot{y}_r s_{tp} \qquad (17)$$

where $\dot{c}_{tp} = -\Theta_p\Omega_p \sin\theta_p cos\Omega_p t$ and $\dot{s}_{tp} = \Theta_p\Omega_p \cos\theta_p cos\Omega_p t$.

CFD SOLVER

Space discretization and numerical integration

The finite volume cell–centered NS COSA code solves the unsteady time–domain RANS and SST equations using structured multi–block grids. COSA uses the compressible flow formulation of the governing equations and low-speed preconditioning to deal with low-speed flows [11, 20, 21]. COSA has

been successfully used to investigate the unsteady hydrodynamics of oscillating wings to extract energy from an oncoming fluid stream [15, 20, 22], the unsteady aerodynamics of Darrieus vertical axis wind turbines [23–25] and the unsteady aerodynamics of fixed-bottom HAWTs in yawed wind [3, 16, 18, 26]. The code also features an efficient harmonic balance solver for the rapid solution of wind turbine unsteady periodic flows, which has been shown to reduce by up to 50 times the runtime for the NS CFD analysis of fixed-bottom HAWT rotors with respect to the conventional time–domain NS method [3]. COSA has also a highly efficient parallelization of both its computing and IO sections [27], distributed-memory (MPI) simulations have been efficiently run with up to 16,000 cluster cores, and the code also features a hybrid parallel architecture for concurrent shared- and distributed-memory computing which enables an optimal exploitation of new multi– and many–core clusters [28].

The COSA discretization of the convective fluxes of both RANS and SST PDEs uses Van Leer's second order upwind MUSCL extrapolations and Roe's flux–difference splitting with Van Albada's flux limiter. The discretization of the diffusive fluxes and the turbulent source terms uses central finite–differencing. The integration of the steady RANS and SST equations is performed in a strongly–coupled fashion using explicit Runge–Kutta time–marching, with local time–stepping, implicit residual smoothing and multigrid for convergence acceleration. TD problems are solved using Jameson's second–order dual–time stepping. Full detail of the space-discretization and the numerical integration of steady and general time-dependent problems can be found in [15].

Calculation of cell face velocities

In rotor flow analyses, COSA computes the cell face velocities $\underline{u}_b$ in Eq. (2) using the freestream–capturing geometric formulation (FCGF) of [29] to ensure global conservation for time–dependent flows. In finite-volume NS CFD codes like COSA, the construction of the convective fluxes in the case of moving grid problems, requires the calculation of the component of cell face velocity u_{bn} along the normal to the cell face itself. The general mathematical definition of u_{bn} is:

$$u_{bn} = \underline{u} \cdot \underline{n} \tag{18}$$

where $\underline{n}$ denotes the unit vector normal to the cell face dS and thus $d\underline{S} = \underline{n}dS$. When analyzing HAWT rotor flows with grids having some degree of skewness and/or distortion, however, it was observed that the direct application of Eq. (18) (with $\underline{u}_b$ defined by Eq. (3)) does not enable the global conservation of freestream flows. In [29] an alternative numerical calculation of u_{bn} was derived to circumvent this issue. The FCGF starts by defining the so-called first area moment of the cell face

$$d\underline{M} = \underline{r} \times d\underline{S} \tag{19}$$

In the case of fixed-bottom HAWT rotors, the normal cell face velocity can then be shown to be:

$$u_{bn} = \underline{\Omega} \cdot d\underline{M}/dS \tag{20}$$

Calculating the area moments of the quadrilateral cell faces as indicated in [29] yields the FCGF. For fixed-bottom HAWT rotor flows, both Eq. (18) and Eq. (20) are available. Part of the results below will demonstrate the strong conservation property of the FCGS, and will assess the impact of using this formulation on the accuracy of HAWT rotor CFD analyses.

Low-speed preconditioning

The solution accuracy of density-based CFD codes like COSA decreases in the presence of low-speed flow regions where the local Mach number drops below the threshold of 0.1 [20]. This is due primarily to improper scaling of the numerical dissipation components as the local Mach number tends to zero. When solving the density-based compressible flow equations using iterative integration methods with a CFL constraint (*e.g.* explicit methods), low flow speeds also result in a significant reduction of the residual convergence rate. In inviscid and, to a significant extent, also in high-Reynolds number flows, this occurs because of the large disparity of acoustic and convective speeds. Low-speed preconditioning (LSP) [30] can resolve the accuracy issue by restoring the balance of all terms appearing in the matrix-valued numerical dissipation in the incompressible flow limit, and can improve the converge rate by substantially reducing the disparity of acoustic and convective speeds. Indeed, the re-equalization of the characteristic speeds yields convergence rates which, for inviscid and relatively simple viscous flow problems, are fairly independent of the Mach number [20].

The COSA LSP algorithm was designed and implemented by starting from the preconditioner proposed by Weiss and Smith [31]. One of the unique LSP algorithm implemented in COSA [21] is that it is applied to both the RANS and SST equations, a feature required for using the computationally efficient strongly coupled integration of the two sets of equations also for problems containing low-speed regions. Part of the analyses below will highlight the improvement of the aerodynamic modelling capabilities of the COSA compressible NS code achievable by using LSP for HAWT rotor flows.

VERIFICATION AND VALIDATION

The COSA predictive capabilities of 3D wing and HAWT rotor aerodynamics have been successfully validated against

measured data in [32] and [3] respectively. The test case analyzed in the former article concerns the steady flow past a wing-body configuration, and the unsteady flow resulting from imposed periodic pitching of this aircraft configuration. A very good agreement of measured and computed force coefficients is found. The latter article presents COSA steady flow analyses of the NREL Phase VI rotor flow [12] at wind speeds of 7 and 13 m/s, and unsteady yawed wind analyses for wind speed of 7 m/s and yaw error of 30^o. A thorough comparison of static pressure along the blade, and radial profiles of normal and tangential forces is carried out in both steady and unsteady cases, and an excellent agreement of CFD results and measured data is observed. All simulations were performed in the rotor frame of reference.

Here the test case analyzed in [3] is reconsidered to *a*) validate the new absolute frame COSA implementation of the rotor flow governing equations, and also *b*) assess the reliability of a simplified method for simulating low-speed flows using compressible CFD codes without LSP. The geometry of this two-blade rotor and the selected wall boundary conditions are reported in Fig. 1(a), the airfoil grid at 50 % tip radius is reported in Fig. 1(b), and the computational domain and the selected farfield boundary conditions are reported in Fig. 1(c). The adopted grid has about 4.2 million cells, and the other grid parameters are reported in [3].

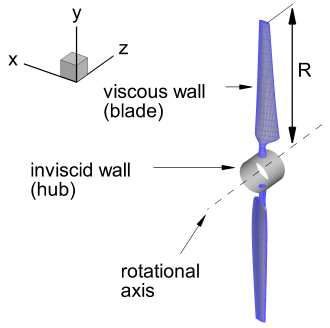

(a) rotor geometry and wall boundary condition.

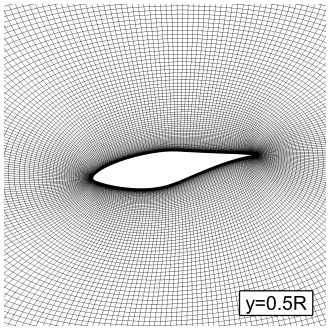

(b) airfoil grid at 50 % tip radius.

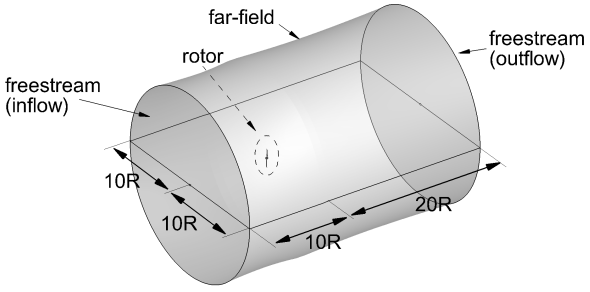

(c) domain dimensions and farfield boundary conditions.

Figure 1. NREL Phase VI HAWT CFD model.

The absolute frame implementation of the governing equations is here validated by considering the NREL Phase VI unsteady rotor flow at 7 m/s with yaw error of 30^o. The top left, top right, bottom left and bottom right plots of Fig. 2 refer respectively to the blade thrust coefficient C_{F_z}, the out–of–plane blade root bending moment coefficient (C_{M_x}), the torsional moment coefficient C_{M_y}, and the blade torque coefficient C_{M_z} (the axial thrust is nondimensionalized by the product of freestream kinetic energy and rotor swept area; moments are nondimensionalized by the product of abovesaid reference force and rotor radius). The curves labeled 'abs HS' are the profiles of these four coefficients during one revolution (values on left axes), and are obtained using the absolute frame formulation. The curves labeled 'rel HS' provide the same coefficients obtained with the relative frame formulation as a percentage (Δ %) of their absolute frame profiles (Δs on right axes). The percentage difference of each coefficient is computed by normalizing the coefficient difference by the RMS of the absolute frame profile. The maximum difference between relative and absolute frame estimates never exceeds 1 %, which confirms the correctness of the absolute frame implementation. These two sets of results are obtained by doubling the freestream velocity but maintaining the tip-speed ratio and Reynolds number of the experiment. This is done to avoid the accuracy losses incurred when using compressible codes to solve low-speed flows when LSP is not available.

This unsteady flow analysis was also performed using the wind speed of the experiment and LSP in the relative frame. The percentage differences of the four coefficients (values on right vertical axes of Fig. 2 plots) computed with this LSP set-up and the reference absolute frame simulation are labeled 'rel LSP' in Fig. 2, which shows that the maximum differences vary between 2 and 3 %. This confirms both the correctness of the LSP implementation, and the validity, for the considered type of problem, of increasing the freestream velocity when the LSP capability is not available.

The contours of static pressure coefficient c_p obtained with the LSP and HS simulations past the blade sections at 30 and 80 % tip radius for $\theta_r = 270^o$ are compared in Fig. 3. The definition of this variable is

$$c_p = \frac{p_\infty - p}{\frac{1}{2}\rho_\infty \left[|\underline{u}^A_\infty|^2 + (\Omega r)^2\right]} \tag{21}$$

where p and p_∞ denote respectively local and freestream static pressure, $\underline{u}^A_\infty$ is the freestream velocity vector and r denotes the radial position along the blade. At $\theta_r = 270^o$ the reference blade considered in Fig. 3 has axis parallel to the ground, and points into the yawed wind. One notes that the LSP c_p contours at 30 % radius are smoother than those of the HS solution, denoting higher quality of the former solution. At 80 % tip radius, the differences between the two solutions are notably smaller because flow speeds are higher and the benefit of using LSP decreases.

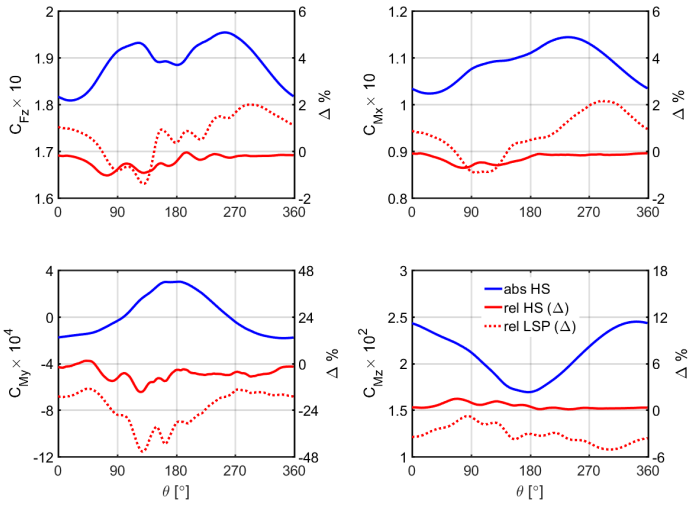

Figure 2. NREL Phase VI HAWT: blade thrust coefficient C_{F_z} (top left), out–of–plane blade root bending moment coefficient (C_{M_x}) (top right), torsional moment coefficient C_{M_y} (bottom left), and blade torque coefficient C_{M_z} (bottom right).

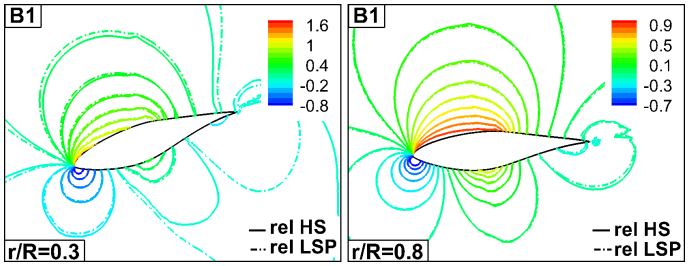

Figure 3. NREL Phase VI HAWT: comparison of static pressure coefficient (c_p) contours past the blade sections at 30 % and 80 % tip radius of blade 1 at $\theta_r = 270^o$ computed with LSP and HS set-ups.

The left portion of Tab. 1 reports mean rotor thrust T and torque M over one revolution in yawed wind (columns with key 'y') using the three considered CFD set-ups. The difference among these values are of the same order of those observed in Fig. 2, as expected. The right portion of the table reports instead the rotor thrust and torque for zero yaw error (columns with key 'zy') computed with the LSP and HS steady CFD set-ups. It is noted that the relative differences between these two output functions are similar to those observed in the unsteady case. It is also interesting to compare the mean power in yawed wind and the steady power in straight wind obtained with the LSP set-up. These two values can be used to estimate the exponent of the cosine of the yaw misalignment. Using the aforementioned values, one finds an exponent of 2.04, lower than the theoretical value of 3. It has been observed in the literature, however, that experimental and numerical analyses indicate a significant dependence of this parameter on the particular test case.

Table 1. NREL Phase VI HAWT: rotor thrust T and torque M in yawed (y) and straight (zy) wind computed with different CFD set-ups.

	rel LSP (y)	rel HS (y)	abs HS (y)	LSP (zy)	HS (zy)
T [N]	922.7	913.3	917.1	1101.2	1113.0
M [Nm]	528.2	510.0	512.7	708.0	707.6

RESULTS

The three-blade HAWT rotor considered herein is that of the NREL 5 MW virtual turbine [13]. This 126 m diameter-rotor has preconing of 2.5^o, shaft tilt of 5^o, rotor overhang of 5 m and tower height of 90 m. The rotor preconing is not included in this study. Steady flow simulations are carried out using different CFD set-ups to investigate the sensitivity of steady rotor aerodynamics to diverse modeling choices. Steady CFD simulations also neglect the effects of the shaft tilt. A pitching FOWT regime of this turbine is also considered, and CFD results are qualitatively compared to those in the literature for the same regime. The rotor geometry and the selected wall boundary conditions are reported in Fig. 4(a), the airfoil grid at 50 % tip radius is reported in Fig. 4(b), and the computational domain and the selected farfield boundary conditions are reported in Fig. 4(c). The choice of the distances of the farfield boundaries from the turbine rotor indicated in Fig. 4(c) was made following the guidelines provided in [33], which reported detailed CFD analyses of the NREL 5 MW rotor using the NASA OVERFLOW 2 RANS code, including analyses of the solution sensitivity to domain size and mesh refinement.

The adopted grid has about 8 million cells, and the minimum distance of the first grid nodes off the blade surface from the blade surface itself is such that the maximum value of the corresponding nondimensionalized wall distance y^+ is less than 1.8 in both steady and time–dependent simulations discussed below. All other grid parameters are reported in [3].

Steady flow analyses

The steady flow simulations in this section refer to a near-rated operating condition characterized by a wind speed of 11 m/s and a rotational speed of 12 RPM. The freestream conditions are characterized by pressure of 1 bar, temperature of 283 K and density of 1.23 Kg/m^3. The solution accuracy improvements achievable by using LSP are considered first. The left image of

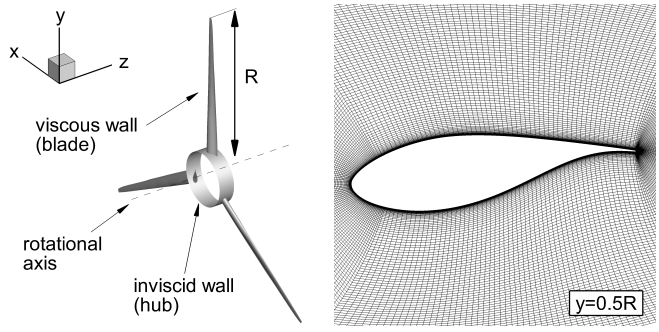

(a) rotor geometry and wall boundary conditions.

(b) airfoil grid at 50 % tip radius.

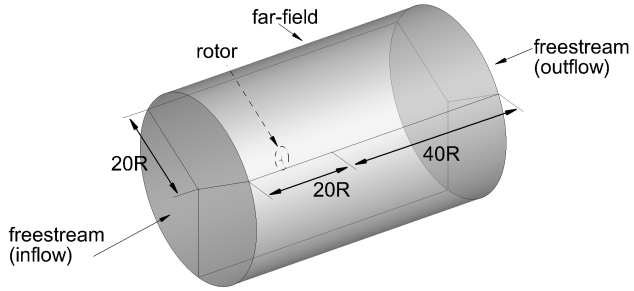

(c) domain dimensions and farfield boundary conditions.

Figure 4. NREL 5 MW HAWT CFD model.

Fig. 5 compares the contours of static pressure coefficient computed with low-speed preconditioning (contours labeled LSP) and without (contours labeled NP) at the blade section at 30 % tip radius, and it clearly highlights a significantly better quality of the LSP solution, whose contours are substantially more regular than those obtained with the standard compressible solver. The right image of Fig. 5 provides the same type of comparison for the section at 80 % tip radius, and it also highlights an improvement of the LSP over the NP solution. The improvement is less significant than at the lower-radius section, because the relative Mach numbers at 80 % tip radius are higher than 0.1, and the accuracy loss of the default compressible solver is thus lower. The first row of Tab. 2 reports the out–of–plane blade root bending moment (M_x), the blade torsional moment (M_y), the rotor thrust (T) and the rotor power (P) obtained by integrating the pressure and viscous blade forces computed by the baseline CFD solver without LSP, whereas the second row reports the values of these parameters obtained using the LSP–enhanced solver. The largest difference between the two result sets is that in rotor power of about 4.5 %, which shows that, in this case, the impact of using LSP on the integral load predictions is not substantial.

The contours of static pressure coefficients past the 30 % and 80 % blade sections obtained with the LSP simulation and a simulation without LSP but using a freestream velocity doubled with respect to the actual one (the latter analysis uses the same

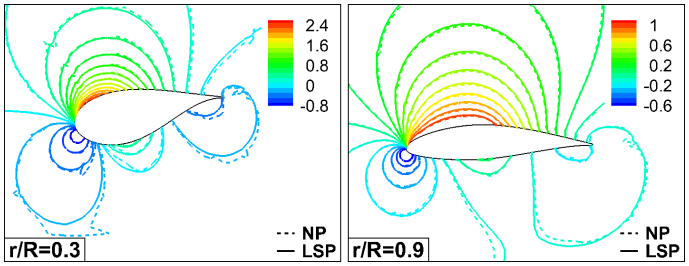

Figure 5. NREL 5 MW HAWT: comparison of static pressure coefficient (c_p) contours past the blade sections at 30 % and 80 % tip radius computed with and without LSP.

tip-speed ratio and the same Reynolds number of the former) are compared in Fig. 6. Cross comparing these results with those of Fig. 5 it is observed that the use of a higher freestream velocity improves the local resolution, but not to the extent achieved by using LSP and keeping the true wind velocity. The values of the blade moments, and the rotor thrust and power obtained with the increased speed simulation are reported in the third row of Tab. 2. One sees that, although the rotor power predicted by the high-speed simulation differs by about 5 % from the LSP estimate, the blade torsional moment M_y predicted by the high-speed simulation differs by more than 10 % with respect to the reference LSP analysis, which is a significant limitation of using the results of high-speed analyses for design applications.

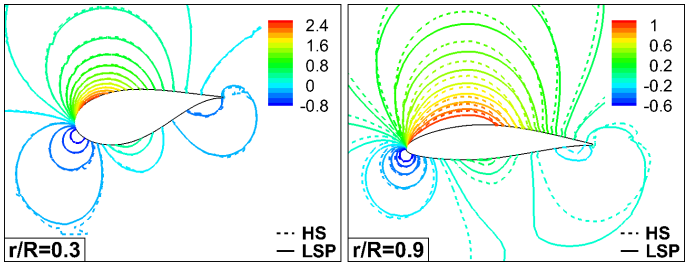

Figure 6. NREL 5 MW HAWT: comparison of static pressure coefficient (c_p) contours past the blade sections at 30 % and 80 % tip radius computed with LSP and HS set-ups.

In all steady simulations discussed thus far, the cell face velocities were computed using the FCGF expressed by Eq. (20). To assess the solution sensitivity to the numerical method used for calculating the cell face velocities, the LSP simulation was repeated calculating the cell face velocities with the standard formulation of Eq. (18). It was found that such LSP solution differs negligibly from that using Eq. (20) for computing cell face velocities. This is also highlighted by the fact that the blade moments, rotor thrust and power of the former solution (row of Tab. 2 labeled 'LSP*') differ negligibly from those of the LSP simulation

using the FGCF (row of Tab. 2 labeled 'LSP'). This result indicates that for fixed-bottom turbine rotor flows, it may not be necessary to undertake the additional code development work to implement the FCGF.

The last row of Tab. 2 also reports the FAST estimates of out–pf–plane root bending moment, rotor thrust and power (the blade torsional moment is presently not readily available in FAST), which are respectively 6.6, 3.2 and 5.6 % higher than the reference LSP estimates, and therefore in reasonably good agreement with this CFD prediction.

Table 2. NREL 5 MW HAWT: blade moments M_x, M_y, rotor thrust T and rotor power P computed with different CFD set-ups.

	M_x [kNm]	M_y [kNm]	T [kN]	P [MW]
NP	8859	89.2	663	4.36
LSP	8900	87.2	663	4.57
HS	8764	75.7	655	4.28
LSP*	8903	87.3	663	4.57
FAST	9489	—	687	4.84

FOWT flow analyses

The pitching FOWT set-up considered herein has the same freestream conditions and rotational speed of the steady flow analyses presented above, and is characterized by pitching amplitude $\Theta_p = 4^o$, pitching centre located at the tower base ($y_{pc} = -90\ m$), pitching angular frequency $\Omega_p = 0.4\pi\ rad/s$, which equals the angular frequency of the rotor speed, and $\phi_p = 180^o$. Blade flexibility effects are not considered, and the blade pitch is fixed throughout the unsteady simulation. The rotor overhang ($z_{pc} = 5\ m$) is included in the analysis, as well as the shaft tilt of 5^o. The TD CFD simulation is carried out in the absolute frame of reference in which the blades rotate past the rotor center and pitch past an axis at the tower base normal to the tower with the prescribed motion. The shaft tilt is accounted for by inclining the oncoming steady wind by 5^o on the horizontal direction, rather than by tilting the rotor upwards by the same amount before generating the CFD grid. No speed scaling is adopted and the simulation is performed using LSP. The cell face velocities were computed using the standard formulation of Eq. (18) rather than the FCGF of Eq. (20).

The aforementioned pitching FOWT regime is one of the most challenging ones analyzed with a FLUENT incompressible flow simulation using a combination of absolute and reference frame set-ups (FLUENT Multiple Reference Frame (MRF) feature) in [4]. As reported in that article, the wave frequency of 0.2 Hz is on the high end of the sea state frequency range in which FOWTs are expected to operate. The considered FOWT operating condition was chosen to have an initial term of comparison for the COSA analyses below, and to consolidate interest in a realistic virtual FOWT test case usable by other researchers to validate alternative high-fidelity and engineering codes.

The time–dependent periodic profiles of rotor power and thrust computed by the COSA compressible simulation over two consecutive periods are reported in the left and right plots of Fig. 7 respectively. The profiles of the same variables computed by FAST, and the peak values obtained with the FLUENT analyses of [4] are also reported.

The overall patterns of the COSA and FAST power profiles are qualitatively similar, but the 15.4 MW–peak power of the COSA analysis is higher than both the FAST peak of 14.1 MW and the FLUENT peak of about 12.5 MW, resulting in the COSA estimate being about 23 % higher than the FLUENT estimate. It is also noted that the FAST peak power observed here is about 1 MW lower than that of the FAST analysis of [4], which would point to a good agreement of the peak power of COSA and the cited FAST analysis. It is also noted that the mean power over one pitching cycle predicted by COSA (about 6.0 MW) is about 30 % higher than the steady state power predicted by the same CFD code. This ratio is of the same order of magnitude of those for similar compressible flow CFD analyses of a 10 MW FOWT pitching with amplitudes between 3^o and 5^o reported in [10].

The overall patterns of the COSA and FAST thrust profiles are also qualitatively similar. However, the $1,100$ KN–peak thrust of the COSA analysis is lower than the FAST peak of $1,235$ kN but similar to the FLUENT peak, resulting in the FAST estimate being about 12 % higher than both CFD estimates. The peak thrust of the present FAST analysis and that of [4] are comparable.

Possible reasons for the discrepancies between the power levels of the present CFD results and the FLUENT incompressible flow analyses in [4] include: A) different levels of mesh refinement. Although the grid used herein has 8 million cells and that used in [4] has about 6 million elements, the size of the cylindrical physical domain used herein is significantly larger than that used in the FLUENT analyses (about 6 times wider in the radial direction and 3 times longer in the axial direction), which results in the overall mesh refinement used herein being lower. The size of the physical domain should be selected so as to minimize the effect of spurious reflections due to the proximity of farfield boundaries and rotor. This is an important aspect affecting the trade-off of accuracy and computational cost of HAWT rotor CFD analyses. As mentioned, the size of the NREL 5 MW turbine rotor domain used herein was determined following the guidelines of [33], and it was not investigated whether a smaller domain size could be used without altering significantly the predicted rotor aerodynamics; B) different

time–integration set-up. The COSA simulation used a second order time-integration with a time–step corresponding to one degree of rotor revolution, whereas the FLUENT simulations used first order time–integration with a time–step corresponding to 2^o of rotor revolution. The COSA FOWT simulation was also repeated using a time–step corresponding to 2^o, and no significant differences with respect to the reported COSA results were observed. However, the use of a second– or first–order time–integration scheme with a given time–step may still result in significant solution differences. Therefore this remains a possible discrepancy source to be further investigated. *C*) compressibility effects. As highlighted below, the maximum relative Mach number for this test case is well above the compressibility threshold of 0.3, due to the tower motion–induced rotor velocities. Relatively small changes in the direction of the relative stream, particularly in the outboard blade, may lead to significant changes of shaft torque. This assumption seems to be corroborated by the fact that the COSA/FLUENT/FAST agreement of peak rotor thrust is higher than that of peak rotor power.

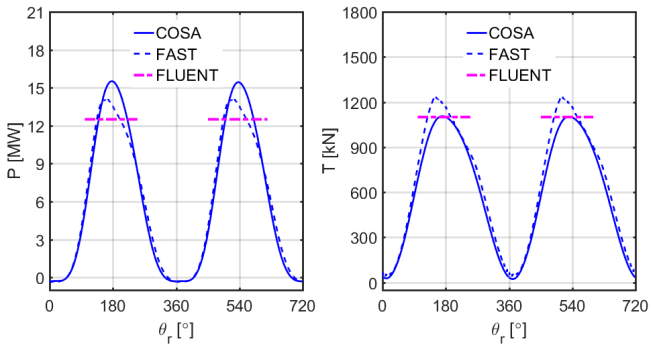

Figure 7. NREL 5 MW HAWT in FOWT pitching ($\Theta_p = 4^o$, $\Omega_p = 0.4\pi$ Hz, $y_{pc} = -90$ m, $z_{pc} = 5$ m): comparison of COSA and FAST rotor thrust (left) and rotor power (right) over two consecutive periods. FLUENT peak levels are from [4]

Figure 8 presents the Mach contours past the 30 % blade section (left) and the 90 % blade section at $\theta_r = 0^o$, when the tower is vertical and has maximum backward velocities decreasing with height, and the reference blade (blade 1) at θ_r is also vertical and above the tower. Due to the high entrainment velocity due to the FOWT pitching, the axial component of the relative speed points against the absolute wind velocity; consequently, the stagnation point moves to the blade upper side, which becomes the pressure side in the pitching FOWT framework. One notes that the higher pressure gradient on the lower side of the examined inboard section yields a moderate flow reversal on the rear lower side, a condition rarely occurring in fixed-bottom turbine rotors.

Figure 9 refers to blade 2, namely the blade at 120^o to the

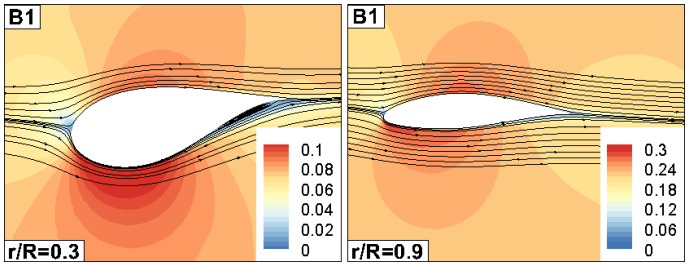

Figure 8. NREL 5 MW HAWT in FOWT pitching ($\Theta_p = 4^o$, $\Omega_p = 0.4\pi$ Hz, $y_{pc} = -90$ m, $z_{pc} = 5$ m): comparison of Mach number contours past the sections at 30 % tip radius (left) and 90 % tip radius (right) of blade 1 at $\theta_r = 0^o$.

reference blade at θ_r moving in the circumferential direction associated with the blade rotation, and presents the Mach contours past the 30 % section (left) and the 90 % section (right) of such blade at $\theta_r = 180^o$. When the rotor is in this position, the tower is vertical and has maximum forward velocity, and blade 2 is at 60^o measured from $\theta_r = 0^o$, featuring fairly high (not maximum, however) forward entrainment velocities. In these conditions, the suction side remains the upper side of the blade, similarly to the case of fixed-bottom HAWT rotors. However, the relative wind speeds are higher (the peak Mach number at the 90 % section is well above 0.4) due to the high entrainment velocity of the tower and its orientation relative to the absolute wind speed. The high level of the relative Mach number past the blade is due primarily to an increase of the angle of attack over the entire blade length. At the inboard sections, this results in fairly high aerodynamic loading, as the blade twist is insufficient to outweigh the higher incidence of the relative flow due to the tower forward speed. This yields a significant amount of stall, as highlighted by the flow separation in the rear of the blade suction side visible in the left plot of Fig. 9. The considered pitching FOWT regime is not the most extreme one in terms of compressible flow effects: the highest relative speeds past the blade would be achieved if one blade were vertical above the tower at $\theta_r = 0^o$. This would occur if $\phi_p = 0^o$ in Eq. (11), rather than 180^o, the value used herein.

All COSA analyses were run on the High End Computing (HEC) service[1] at Lancaster University and the ARCHER UK national supercomputing service[2], and used 256 cluster cores. The discussed TD simulations were run without multigrid, and runtimes varied between 2 and 4 days, depending on the simulation settings, the processor type and the cluster node-networking system.

[1] https://www.lancaster.ac.uk/iss/hec, accessed on 30 June 2018
[2] http://www.archer.ac.uk, accessed on 30 June 2018

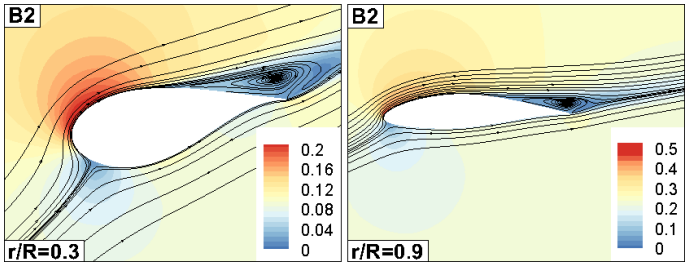

Figure 9. NREL 5 MW HAWT in FOWT pitching ($\Theta_p = 4^o$, $\Omega_p = 0.4\pi\ Hz$, $y_{pc} = -90\ m$ $z_{pc} = 5\ m$): comparison of Mach number contours past the sections at 30 % tip radius (left) and 90 % tip radius (right) of blade 2 at $\theta_r = 180^o$.

CONCLUSIONS

The paper provided a novel contribution to the analysis of the correlation between BEMT and CFD codes for FOWT rotor aerodynamics by analyzing with FAST and compressible flow CFD a pitching FOWT test case analyzed with FAST and incompressible flow CFD in previous independent work. The LSP–enhanced compressible Navier-Stokes COSA code and FAST were used to analyze the unsteady flow regime of a FOWT rotor configuration featuring the NREL 5 MW rotor pitching with amplitude of 4^o and frequency of $0.2\ Hz$. The peak power of the compressible CFD analysis was found to be about 9 % higher than that of FAST, whereas the peak thrust of the same CFD analysis was found to be about 11 % lower than that of FAST. The quantitative differences between the peak power and thrust between the incompressible ANSYS FLUENT and FAST analyses of [4] are similar to those found in the present studt; however, the peaks of both power and thrust of the FLUENT analyses in [4]are lower than the FAST estimates therein, and the compressible CFD peak power is about 20 % higher than its incompressible counterpart. As the instantaneous Mach number at the outboard part of the blades when the tower has maximum forward velocity is found to be well above 0.4, the qualitative differences between compressible and incompressible CFD predictions may be due to compressibility effects, resulting in different time–dependent values of the angle of attack during the pitching cycle. This hypothesis will be validated in future work. Other possible causes include different level of local grid refinement and different domain sizes of the two CFD analyses.

Presented were also the equations solved by COSA in absolute and rotating frames, and two alternative ways of computing cell face velocities, one based on a straightforward discretization of the user–given kinematic laws, the other implementing such laws using freestream capturing area moments to ensure global conservation of the numerical method. Numerical tests based on the steady flow past the NREL 5 MW rotor showed that the solutions obtained using either method differ negligibly. However, the extension of this conclusion to the CFD analysis of FOWT rotors requires new CFD development and testing work. This research question is also relevant to commercial CFD codes, and is a key outstanding source of solution uncertainty.

Future work includes assessing solution quality improvements achievable by using Large Eddy Simulation (LES). The validation of both RANS and LES CFD codes for FOWT rotor unsteady aerodynamics, however, would greatly benefit from the availability of high–quality measured data of model and, even more, full-scale FOWT rotor aerodynamic data.

ACKNOWLEDGMENT

Lancaster University is gratefully acknowledged for allowing use of the HEC cluster for the research reported herein. The authors also thank EPSRC for providing access to computational resources on ARCHER through the UK Applied Aerodynamics Consortium Leadership Project e529.

REFERENCES

[1] Jonkman, J., and Martha, D., 2011. "Dynamics of offshore floating wind turbinesanalysis of three concepts". *Wind Energy,* ***14***, pp. 557–569.

[2] Bak, C., 2013. "Aerodynamic design of wind turbine rotors". In *Advances in wind turbine blade design and materials*, W. Gentzsch and U. Harms, eds., Vol. 47 of *Energy*. Woodhead Publishing, Cambridge, UK, pp. 59–108.

[3] Drofelnik, J., Da Ronch, A., and Campobasso, M., 2018. "Harmonic balance Navier-Stokes aerodynamic analysis of horizontal axis wind turbines in yawed wind". *Wind Energy,* ***21***(7), pp. 515–530. DOI: 10.1002/we.2175.

[4] Tran, T.-T., and Kim, D.-H., 2015. "The platform pitching motion of oating offshore wind turbine: A preliminary unsteady aerodynamic analysis". *Journal of Wind Engineering and Industrial Aerodynamics,* ***142***, pp. 65–81.

[5] Sebastian, T., and Lackner, M., 2013. "Characterization of the unsteady aerodynamics of offshore oating wind turbines". *Wind Energy,* ***16***, pp. 339–352.

[6] Tran, T.-T., and Kim, D.-H., 2016. "CFD study into the influence of unsteady aerodynamic interference on wind turbine surge motion". *Renewable Energy,* ***90***, pp. 204–228.

[7] Jonkman, J. FAST: An aeroelastic computer-aided engineering (CAE) tool for horizontal axis wind turbines. https://nwtc.nrel.gov/FAST, accessed on 22 April 2018.

[8] Tran, T.-T., and Kim, D.-H., 2016. "Fully coupled aerohydrodynamic analysis of a semi-submersible fowt using a dynamic uid body interaction approach". *Renewable Energy,* ***92***, pp. 244–261.

[9] Liu, Y., Xiao, Q., Incecik, A., Peyrard, C., and Wan, D., 2017. "Establishing a fully coupled CFD analysis tool for floating offshore wind turbines". *Renewable Energy,* ***112***, pp. 280–301.

[10] Leble, V., and Barakos, G., 2017. "10-MW Wind Turbine Performance Under Pitching and Yawing Motion". *Journal of Solar Energy Engineering,* ***139***, August.

[11] Campobasso, M., Yan, M., Drofelnik, J., Piskopakis, A., and Caboni, M., 2014. Compressible Reynolds-Avergaed Navier-Stokes Analysis of wind Turbine Turbulent Flows Using a Fully Coupled Low-Speed Preconditioned Multigrid Solver. ASME paper GT2014-25562, June.

[12] Hand, M. M., Simms, D. A., Fingersh, L. J., Jager, D. W., Cotrell, J. R., Schreck, S., and Larwood, S. M., 2001. Unsteady Aerodynamics Experiment Phase VI: Wind Tunnel Test Configurations and Available Data Campaigns. Tech. Rep. NREL/TP-500-29955, NREL, Golden, CO, USA, Dec.

[13] Jonkman, J., Butterfield, S., Musial, W., and Scott, G., 2009. Definition of a 5-MW Reference Wind Turbine for Offshore System Development. Tech. Rep. NREL/TP-500-38060, NREL, Golden, CO, USA.

[14] Menter, F., 1994. "Two-equation Turbulence-models for Engineering Applications". *AIAA Journal,* ***32***(8), August, pp. 1598–1605.

[15] Campobasso, M., Piskopakis, A., Drofelnik, J., and Jackson, A., 2013. "Turbulent Navier-Stokes Analysis of an Oscillating Wing in a Power-Extraction Regime Using the Shear Stress Transport Turbulence Model". *Computers and Fluids,* ***88***, December, pp. 136–155.

[16] Campobasso, M., Drofelnik, J., and Gigante, F., 2016. "Comparative Assessment of the Harmonic Balance Navier-Stokes Technology for Horizontal and Vertical Axis Wind Turbine Aerodynamics". *Computers and Fluids,* ***136***, pp. 345–370.

[17] Da Ronch, A., McCracken, A., Badcock, K., , Widhalm, M., and Campobasso, M., 2013. "Linear Frequency Domain and Harmonic Balance Predictions of Dynamic Derivatives". *Journal of Aircraft,* ***50***(3), pp. 694–707.

[18] Campobasso, M., Gigante, F., and Drofelnik, J., 2014. Turbulent Unsteady Flow Analysis of Horizontal Axis Wind Turbine Airfoil Aerodynamics Based on the Harmonic Balance Reynolds-Averaged Navier-Stokes Equations. ASME paper GT2014-25559, June.

[19] Chen, J., Ghosh, A., Sreenivas, K., and Whitfield, D., 1997. Comparison of computations using Navier-Stokes equations in rotating and fixed coordinates for flow through turbomachinery. 35th Aerospace Sciences Meeting and Exhibit, January. Reno, NV, U.S.A.

[20] Campobasso, M., and Drofelnik, J., 2012. "Compressible Navier-Stokes analysis of an oscillating wing in a power-extraction regime using efficient low-speed preconditioning". *Computers and Fluids,* ***67***, August, pp. 26–40.

[21] Campobasso, M., Yan, M., Bonfiglioli, A., Gigante, F., Ferrari, L., Balduzzi, F., and Bianchini, A., 2018. "Low-speed preconditioning for strongly coupled integration of Reynolds-averaged Navier-Stokes equations and two-equation turbulence models". *Aerospace Science and Technology,* ***77***, pp. 286–298.

[22] Drofelnik, J., and Campobasso, M., 2016. "Comparative Turbulent Three-Dimensional Navier-Stokes Hydrodynamic Analysis and Performance Assessment of Oscillating Wings for Renewable Energy A pplications". *International Journal of Marine Energy,* ***16***, pp. 100–115.

[23] Balduzzi, F., Bianchini, A., Gigante, F., Ferrara, G., Campobasso, M., and Ferrari, l., 2015. Parametric and Comparative Assessment of Navier-Stokes CFD Technologies for Darrieus Wind Turbines Performance Analysis. GT2015-42663, June.

[24] Balduzzi, F., Drofelnik, J., Bianchini, A., Ferrara, G., Ferrari, L., and Campobasso, M., 2017. "Darrieus wind turbine blade unsteady aerodynamics: a three-dimensional Navier-Stokes CFD assessment". *Energy,* ***128***, pp. 550–563.

[25] Balduzzi, F., Marten, D., Bianchini, A., Drofelnik, J., Ferrari, L., Campobasso, M., Pechlivanoglou, G., Nayari, C., Ferrara, G., and Paschereit, C., 2018. Three-Dimensional Aerodynamic Analysis of a Darrieus Wind Turbine Blade Using Computational Fluid Dynamics and Lifting Line Theory.

[26] Campobasso, M., and Baba-Ahmadi, M., 2012. "Analysis of Unsteady Flows Past Horizontal Axis Wind Turbine Airfoils Based on Harmonic Balance Compressible Navier-Stokes Equations with Low-Speed Preconditioning". *Journal of Turbomachinery,* ***134***(6), November.

[27] Jackson, A., Campobasso, M., and Drofelnik, J., 2018. "Load balance and parallel I/O: Optimising COSA for large simulations". *Computers and Fluids*, March.

[28] Jackson, A., and Campobasso, M., 2011. "Shared-memory, Distributed-memory and Mixed-mode Parallelization of a CFD Simulation Code". *Computer Science Research and Development,* ***26***(3-4), pp. 187–195.

[29] Obayashi, S., 1992. "Freestream capturing for moving coordinates in three dimensions". *AIAA Journal,* ***30 (4)***, pp. 1125 – 1128.

[30] Turkel, E., 1987. "Preconditioned methods for solving the incompressible and low speed compressible equations". *Journal of Computational Physics,* ***72***, pp. 277–298.

[31] Weiss, J., and Smith, W., 1995. "Preconditioning applied to variable and constant density flows". *AIAA Journal,* ***33***(11), pp. 2050–2057.

[32] Drofelnik, J., Da Ronch, A., and Campobasso, M., 2018. Feasibility of the Navier-Sokes harmonic balance method for modelling aircraft unsteady aerodynamics. ICAS paper ICAS2018-0791, September. Belo Horizonte, Brazil.

[33] Chow, R., and van Dam, C., 2012. "Verication of computational simulations of the NREL 5 MW rotor with a focus on inboard ow separation". *Wind Energy,* ***15***, pp. 967–981.